Elucidating the Impact of Molecular Weight on Morphology, Charge Transport, Photophysics and Performance of All-Polymer Solar Cells

ARTICLE

Elucidating the Impact of Molecular Weight on Morphology, Charge Transport, Photophysics and Performance of All-Polymer Solar Cells

Duyen K. Tran,[a,†] Amélie Robitaille,[b,†] I. Jo Hai,[c] Xiaomei Ding,[a] Daiki Kuzuhara,[d]

Tomoyuki Koganezawa,[e] Yu-Cheng Chiu,[c] Mario Leclerc,[*,b] Samson A. Jenekhe[*,a]

Understanding the influence of polymer molecular weight on the morphology, photophysics, and photovoltaic properties of polymer solar cells is central to further advances in the design, processing, performance and optimization of the materials and devices for large scale applications. We have synthesized six number-average molecular weight (M_n) values (21-127 kDa) of biselenophene-naphthalenediimide copolymer (PNDIBS) via direct heteroarylation polymerization and used them to investigate the effects of the acceptor polymer molecular weight on the charge transport, blend photophysics, blend morphology, and photovoltaic properties of all-polymer solar cells (all-PSCs) based on PNDIBS and the donor polymer PBDB-T. The short-circuit current and power conversion efficiency (PCE) of the PBDB-T:PNDIBS blend devices were found to increase with increasing M_n until reaching peaks at an optimal molecular weight of 55 kDa and then decreased with further increases in M_n. The maximum PCE of 10.2% observed at the optimal M_n value of 55 kDa coincided with optimal blend charge transport properties, blend photophysics, and blend morphology at this critical molecular weight. Compared to the bi-continuous network of ~5.5-6.5 nm crystalline domains with predominantly *face-on* molecular orientations observed at 55 kDa, a relatively disordered microstructure with larger scale phase separation was evident at higher M_n while more finely packed crystalline domains were seen at 21 kDa. The sensitivity of the device efficiency to the active layer thickness was found to also depend on the PNDIBS M_n value. These results highlight the importance of tuning the molecular weight of the polymer components to optimize the morphology, charge transport, photophysics and efficiency of all-polymer solar cells. The results also provide new insights on structure-property relationships for a promising n-type semiconducting copolymer.

Introduction

Advances in molecular design of materials and device engineering strategies have enabled substantial progress in raising the efficiency of organic photovoltaics (OPVs) over the past several years.[1-36] Among the various OPV technologies, all-polymer solar cells (all-PSCs) where the photoactive layer is composed of a blend of an electron-donating (donor) conjugated polymer and an electron-accepting (acceptor) conjugated polymer – the so-called bulk heterojunction (BHJ) architecture – offer unique advantages, including the facile tuning of optoelectronic properties of polymers,[1-36] their superior photochemical stability,[33, 37, 38] their excellent durability under thermal and mechanical stresses,[35, 39-44] and

their potential for large scale manufacture.[30, 40] These features of all-PSCs make them especially appealing candidates for commercial applications in many areas. Although the power conversion efficiency (PCE) of all-PSCs has recently exceeded 10-11% in several different binary blend systems,[17, 25, 26, 28, 29, 31-33, 36] it lags behind the PCE of small-molecule non-fullerene acceptors (SM-NFAs) based solar cells where the PCEs has reached over 16%.[45-47] From a device engineering perspective, the major bottlenecks hindering further advances in the photovoltaic performance of all-PSCs include the low photocurrent density (J_{sc})[1-4, 12, 13, 15-17, 21, 30] and low fill factor (FF).[1-4, 19, 21, 30] The photocurrent is limited by the low electron mobility of the acceptor polymer component and the overall lack of greater complementary light-harvesting of the solar light by both blend components.[1-4, 12, 13, 15-17, 21, 30] The small fill factor is primarily due to the non-optimal blend morphology, which in turn is influenced by polymer molecular weight[10, 11, 14, 18, 22] and polymer/polymer interchain interactions.[9, 13, 19, 26, 30]

Advancing all-PSCs from a materials chemistry point of view, includes not only finding ways to harvest more of the solar spectrum,[12, 18, 29, 31, 32] increase the carrier mobilities of the donor and acceptor conjugated polymers,[18, 25, 31, 32] and to control and fine-tune the blend morphology[9, 13, 19, 26, 30, 48] and blend photophysics[31, 34, 43] but also to understand the

[a.] Department of Chemical Engineering and Department of Chemistry, University of Washington, Seattle, Washington 98195-1750, United States
[b.] Département de Chimie, Université Laval, Québec City, Québec G1V 0A6, Canada
[c.] University of Science and Technology (TAIWAN TECH) No. 43, Section 4, Keelung Rd, Da'an District, Taipei City, Taiwan 106
[d.] Faculty of Science and Engineering, Iwate University, 4-3-5 Ueda, Morioka, Iwata, 020-8551, Japan
[e.] Industry Application Division, Japan Synchrotron Radiation Research Institute, Sayo, Hyogo, 679-5198, Japan
† These authors contributed equally.

underlying structure-property-performance relationships. A fundamental molecular parameter that can substantially influence the physical properties of the component materials, the thermodynamics of all-polymer blends, and the efficiency of all-PSCs is polymer molecular weight.[1, 10, 11, 14, 18, 22, 49, 50] Although several prior studies have been devoted to the effects of the molecular weights of the acceptor polymer and donor polymer on the photovoltaic properties of all-polymer solar cells, the results gave rise to divergent conclusions.[10, 11, 14, 18, 22, 49, 50] It was found that increasing the molecular weight of either the donor polymer or the acceptor polymer led to significantly enhanced power conversion efficiency (PCE) of all-PSCs due to the synergistic improvement of the short-circuit current (J_{sc}) and the fill factor (FF) while the open-circuit voltage (V_{oc}) remained relatively constant.[10, 11, 18, 49, 50] In contrast, other reports have found simultaneous drop in both J_{sc} and FF, and thus the power conversion efficiency, with increasing polymer molecular weight.[14, 22] The decline of J_{sc} and FF with increasing molecular weight was attributed to non-optimal blend morphology featuring either coarser domains due to large liquid-liquid phase separations[22] or greater molecular miscibility between the blend components,[14] both of which led to increased charge recombination and poorer charge photogeneration and charge extraction rates. Among the limitations of these prior studies of the impact of the number-average molecular weight (M_n) on the performance of all-PSCs include the relatively narrow range of M_n of the polymers investigated. Very few of these studies reported M_n values measured at high temperature (> 100 °C)[14, 22, 49] and hence the effects of actual molecular weight of the conjugated polymer could not be delineated from those due to effects of chain aggregation.[11, 14, 18, 50] Nearly all prior studies, except one,[22] were focused on the acceptor polymer poly([N,N'-bis(2-octyldodecyl)-naphthalene-1,4,5,8-bis(dicarboximide)-2,6-diyl]-alt-5,5'-(2,2'-bithiophene)) (PNDIOD-T2 or N2200) and various non-high performing donor polymers.[10, 14, 49, 50]

Towards the resolution of the current conflicting views on how polymer molecular weight impacts the photovoltaic properties of all-PSCs,[10, 11, 14, 22, 49, 50] we aim to address this problem by employing an entirely new binary blend system whose components have not previously been involved in studies of the effects of M_n, including the well-known high-performance donor polymer, poly[(2,6-(4,8-bis(5-(2-ethylhexyl)thiophen-2-yl)-benzo[1,2-b:4,5-b']dithiophene))-alt-(5,5-(1',3'-di-2-thienyl-5'.7'-bis(2-ethylhexyl)benzo[1',2'-c:4',5'-c']dithiophene-4,8-dione], (PBDB-T) (Figure 1a).[51] We decided to focus on the direct heteroarylation polymerization (DHAP)-prepared poly([N,N'-bis(2-octyldodecyl)-naphthalene-1,4,5,8-bis(dicarboximide)-2,6-diyl]-alt-5,5'-(2,2'-biselenophene)) (PNDIBS) (Figure 1a) as the acceptor polymer component in the proposed M_n dependent studies. DHAP has been shown to be a simple and environmental-friendly pathway to synthesize highly efficient organic photovoltaic materials with minimal structural defects.[52-56] Compared to previously well-studied N2200,[10, 14, 49, 50] our group has shown Stille-derived PNDIBS, which incorporates biselenophene units instead of bithiophene units, to have a narrower optical bandgap, increased crystallinity, and enhanced bulk charge transport and photovoltaic properties.[18, 26, 57] Thus well-defined DHAP-derived PNDIBS of sufficiently broad range of M_n values can be expected to advance our understanding of the impact of molecular weight on photovoltaic properties while enabling development of high performance all-PSCs.

In this paper, we report a comprehensive investigation of the effects of the number-average molecular weight (M_n) of the acceptor polymer on the blend charge transport, blend photophysics, blend morphology, and photovoltaic properties of all-PSCs. The binary blend devices paired the donor polymer PBDB-T respectively with the DHAP-prepared acceptor copolymer PNDIBS at six different M_n values from 21 to 127 kDa. We found that the key photovoltaic parameters of the PBDB-T:PNDIBS blend devices, PCE and J_{sc}, both increased with increasing M_n until reaching peaks at an optimal molecular weight of 55 – 66 kDa and subsequently decreased with further increases in M_n. The observed peak in photovoltaic performance at M_n of 55 kDa coincided with an optimal blend morphology composed of a bi-continuous network of ordered crystalline features of predominantly *face-on* molecular orientations and 5.5-6.5 nm domain sizes. The optimal or critical M_n value also marked peaks in charge photogeneration rate and symmetric charge transport. Outside of the optimal M_n range, the blend morphology evolved from finely and tightly packed in the 21 kDa blends to disordered and amorphous structures with large phase separation, leading to severe charge recombination and space-charge build-up, which are detrimental to photovoltaic device performance. At the critical M_n value of 55 kDa, the all-PSCs had a maximum PCE of 10.2% with an average of 9.3% as a result of the favorable blend charge transport properties, blend photophysics, and blend morphology. We also found that the M_n has a significant impact on the sensitivity of the device efficiency to the active layer thickness. While the PCE of the optimal M_n was rather insensitive to the active layer thickness, the efficiency of all-PSCs at the higher M_n was
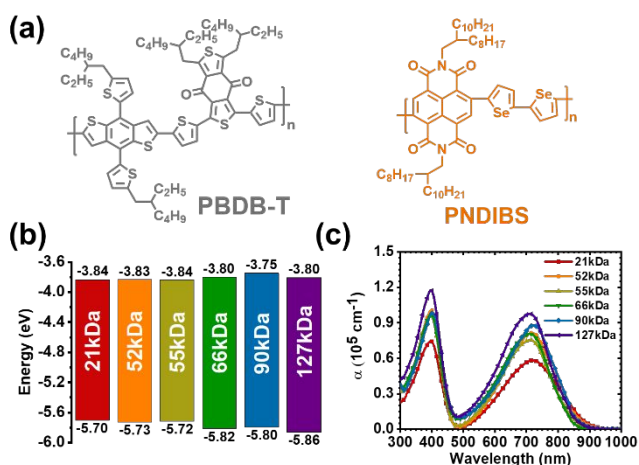

Figure 1. (a) Molecular structures of donor polymer (PBDB-T) and acceptor polymer (PNDIBS). (b) HOMO/LUMO energy levels of the acceptor polymer of varying number-averaged molecular weight M_n. (c) Thin-film optical absorption spectra of the PNDIBS acceptor copolymer at different number-average molecular weights M_n.

strongly dependent on the layer thickness and in this case, the thinner photoactive layer afforded the highest PCE. Overall, this study and results provide a broader and unified understanding of how the molecular weight of a polymer component of all-polymer solar cells impacts the blend charge transport, blend photophysics, blend morphology, and photovoltaic properties as well as give new structure-property relationships for a promising n-type semiconducting copolymer.

Experimental Methods

Materials. Naphthalene-1,4,5,8-tetracarboxylic dianhydride was obtained from TCI America and used without any further purification. Selenophene, tris(dibenzylideneacetone) dipalladium (0), pivalic acid, cesium carbonate and other precursors for the preparation of the 2-octyl-1-dodecylamine were obtained from Sigma-Aldrich and used without further purifications. Extra dry chlorobenzene was obtained from Accros Organic and de-gassed with Argon for 15 min prior to utilization. Other starting materials were purchased from Sigma-Aldrich, TCI America or Alfa Aesar. The donor polymer PBDB-T was synthesized in our lab.

Synthesis of Materials. The preparation of the 2,6-dibromonaphthalene-1,4,5,8-diimide monomer was realized following to the literature approach.[50] The preparation of 2,2'-biselenophene (Figure S1), was performed according to the conditions of the literature.[54] Then, a further step was taken to obtain the 5,5'-bistrimethylstannyl-2, 2'-biselenophene (Figure S2).[54, 55] The DHAP and Stille protocols for the polymer synthesis were performed according to the literature methods.[50, 54] The details are given in the SI.

Fabrication and Characterization of all-PSCs. Solar cells devices were fabricated with an inverted architecture of ITO/ZnO/PEI/Blend/MoO₃/Ag. ITO-coated substrates (15 Ω/square, Shanghai B. Tree Tech, Shanghai, China) were cleaned sequentially in ultrasonic baths with acetone, deionized water, and isopropyl alcohol for 30 min, dried using nitrogen gas, and followed by 10 mins of O_2 plasma cleaning. The ZnO precursor solution was spin-coated onto the ITO and followed by thermal annealing at 250 °C for 30 min to make ~30 nm thick ZnO layer. A 0.05 wt% solution of polyethylenimine (PEI) in 2-methoxyethanol was spin-coated onto the ZnO layer and dried at 120 °C for 10 min. The PBDB-T:PNDIBS (1:0.8 wt/wt) blends were prepared in chlorobenzene, mixed and stirred overnight at 85°C in the glovebox. The blend solutions were spin-coated at 1000 rpm for 50s, followed by thermal annealing at 110°C for 10 min in the Argon-filled glovebox. All the active layers had a thickness of 105 ± 5 nm. MoO₃ (0.5 nm) and Ag (100 nm) were thermally deposited onto the active layer. An aperture mask with area of 3.14 mm² was applied during measurements to define the illuminated device area. After evaporation of the electrode, the photovoltaic cells were tested under AM 1.5G solar illumination at 100 mW/cm² in ambient air by using a solar simulator (Model 16S, Solar Light Co., Philadelphia, PA) with a 200W Xenon Lamp Power Supply (Model XPS 200, Solar Light Co., Philadelphia, PA) calibrated by NREL certified Si photodiode (Model 1787-04, Hamamatsu Photonics K.K., Japan) and a

HP4155A semiconductor parameter analyzer (Yokogawa Hewlett Packard, Japan). After the *J-V* measurements, the external quantum efficiency (EQE) spectra were measured by using a solar cell quantum efficiency measurement system (Model QEX10, PV Measurements, Inc., Boulder, CO) with a 2 mm² (2 mm × 1 mm) size masked incident light source and TF Mini Super measurement apparatus for multiple devices in a single substrate. The EQE system was calibrated with a Si photodiode before measurement.

Fabrication and Characterization of SCLC devices. Current-voltage (*J-V*) characteristics of the SCLC devices were measured by using a HP4155A semiconductor parameter analyzer (Yokogawa Hewlett-Packard, Tokyo). The carrier mobility was deduced by fitting the *J-V* curves to the Mott–Gurney equation where J is the current density, ε_o is the permittivity of free space, ε is the relative permittivity, μ is the zero-field mobility, V is the applied voltage, L is the thickness of active layer.

$$J = \frac{9}{8}\varepsilon_0\varepsilon\mu\frac{V^2}{L^3}$$

The SCLC device structures for electron-only and hole-only were ITO/ZnO/PEI/Blend/LiF (1nm)/Al (100nm) and ITO/PEDOT: PSS/Blend/MoO₃ (7.5nm)/Ag (100nm), respectively. Each active layer of both neat and blend films was processed at the optimized all-PSC devices condition as described above and spin-coated at 1000 rpm for 50s and followed by thermal annealing at 110°C for 10 min inside glovebox.

Fabrication and Characterization of OFETs. TFT devices were fabricated on highly doped n-type Si (100) wafer with a 300 nm thick SiO₂ treated with self-assembled monolayer of n-octadecyltrimethoxysilan (OMTS), according to the reported method.[56] Before use, the OTMS monolayer was rinsed subsequently with toluene, acetone, and isopropyl alcohol and dried under a nitrogen stream. Static water contact angles of the OTMS substrates measured by Edmund Scientific goniometer were higher than 105 degree. The solutions (5 mg/mL) of polymer semiconductor for transistor devices were prepared by dissolving the polymer in chlorobenzene at 80°C for 30 min and then spin-cast on the OTMS substrates with controlled thickness at ~40 nm. The as-prepared thin films were thermally annealed at 170°C for 1 hour in N₂-filled glove box. A top-contact gold electrode (70 nm) was subsequently deposited by evaporation through a shadow mask with a channel length (L) and width (W) defined as 50 and 1000 μm, respectively. The transistor characteristics were measured by Keithley 4200 semiconductor parameter analyzer (Keithley Instruments Inc., Cleveland, OH, USA) in an N₂ filled glove box at room temperature. The effect of molecular weight on μ_e^{FET} can be inferred from the standard FET relation by calculating derivative charge mobility using the equation for I_{ds} in the saturation region.

$$I_{ds} = \frac{WC_i}{2L}\mu(V_{gs} - V_T)^2$$

AFM Imaging. Atomic force microscopy (AFM) characterization of the surface morphology was done on the active layers of the actual polymer solar cells, used in the photovoltaic measurements, by using a Bruker Dimension scanning probe microscope (SPM) system.

GIWAXS. Grazing incidence X-ray scattering (GIWAXS) experiments were conducted at the Japan Synchrotron Radiation Facility SPring-8 by using the beamlines BL46XU. Thin film samples of the neat donor polymer (PBDB-T) and acceptor polymers (PNDIBS) were spin-coated on the top of glass substrates and annealed at 110 °C for 10 min. The binary blend films were prepared in the same manner as the actual all-PSC devices on ZnO/PEI-coated ITO substrates. The X-ray beam was monochromatized by a double-crystal Si (111) monochromator, and the X-ray energy in this experiment was 12.40 keV (λ = 0.1 nm). The angle of incident X-ray to sample surface was 0.12° with a Huber diffractometer. The scattered profile from the film sample was detected using an area detector (PILATUS 300K) for 1 s at room temperature, and the distance between the sample and detector was 175.0 mm. The crystal coherence length (L_c) of samples was determined by using the Scherrer equation: L_c = $2\pi K/\Delta q$, where K is a shape factor (typically 0.89) and Δq is the full width at half-maximum (FWHM) of the diffraction peak. Here, the L_c (100) was obtained from the FWHM of the (100) diffraction peak in the-plane (q_{xy}) line cut.

Results and Discussion

Synthesis and Characterization. The monomers, 2,6-dibromonaphthalene-1,4,5,8-diimide and 2,2'-biselenophene, were synthesized following the conditions reported in the literature, and a detailed protocol is available in the Supporting Information.[53, 57] We have previously reported DHAP-based synthesis of the *bithiophene*-NDI copolymer, PNDIOD-T2, and observed that a more regioregular polymer was achieved than the same polymer made by conventional Stille coupling polymerization.[53] Here, we wanted to confirm the reproducibility and robustness of the DHAP approach by applying it under similar conditions to prepare the *biselenophene*-NDI copolymer, PNDIBS, and by optimization of the DHAP polymerization time to produce a series of polymers with different molecular weights (Table S1). In the case of the Stille-prepared PNDIBS, we used the same conditions reported earlier.[18, 57] Scheme S1 presents the general conditions for the copolymerization of 2,6-dibromonaphthalene-1,4,5,8-diimide and 2,2'-Biselenophene by DHAP and by Stille, respectively.

The ^{1}H NMR spectra of both the Stille and DHAP PNDIBS samples are shown in Figures S3 and S4. Despite the limited solubility of both polymer samples in 1,1,2,2-tetrachloroethane-D2, the spectra are clear enough to identify structural differences between the two polymers. The DHAP-prepared PNDIBS exhibit a 2:3.98 ratio between the NDI and the biselenophene protons in the aromatic region, which deviate only marginally from the expected ratio of 2:4. On the other hand, the Stille-prepared PNDIBS sample showed a ratio of 2:4.23 between the NDI and biselenophene protons, clearly indicating some homocoupling of the tin derivative monomers. Moreover, the broader peak at 8.6 to 8.75 ppm can be associated to the unbrominated NDI end-groups. The debromation of the NDI monomer has been previously shown to induce the homocoupling of the other monomer, notably the

tin derivative monomer in our Scheme S1.[60] Thermogravimetric analysis (TGA) showed onset degradation temperature (T_d) of over 400ºC (Figure S5) suggesting that the DHAP-prepared PNDIBS polymers had excellent thermal stability. Differential scanning calorimetry (DSC) scans (Figure S6) showed that the DHAP-prepared PNDIBS samples had a higher melting temperature (T_m = 357ºC) compared to the previously reported Stille-prepared PNDIBS of comparable molecular weight.[18] These results clearly indicated that NDI-based copolymers prepared via DHAP method can afford higher regioregularity by minimizing homocoupling defects than the conventional Stille-prepared polymers. The molecular weight and dispersity of the PNDIBS samples were characterized by size exclusion chromatography (SEC) using 1,2,4-trichlorobenzene (TCB) eluent at 110 °C relative to polystyrene standards. The molecular weight data are summarized in Table 1. We note that the solubility of the PNDIBS samples depended on the molecular weight. Specifically, the higher molecular weight samples (M_n > 55kDa) required a higher temperature (T > 80ºC) and longer stirring time to achieve complete dissolution and formation of true solutions.

The electronic structure of the series of PNDIBS of varying molecular weight was characterized in terms of cyclic voltammetry (CV) derived HOMO/LUMO energy levels, which are shown in Figure 1b and summarized in Table 1. The cyclic voltammograms for the reduction and oxidation processes in PNDIBS are shown in Figures S7 and S8, respectively. The HOMO and LUMO energy levels of PNDIBS with M_n of 21 kDa, 52 kDa, and 55 kDa are nearly identical at -5.70 – -5.73 eV and -3.83 – -3.84 eV, respectively. The LUMO energy level of PNDIBS with higher M_n values was slightly upshifted to -3.75 – -3.80 eV. A similar trend was also observed in the HOMO energy levels of the higher molecular weight PNDIBS, where the HOMO downshifted -5.80 – -5.86 eV (Figure 1b). These HOMO/LUMO energy levels of PNDIBS are comparable to literature results.[18, 57] More interestingly, the large range of M_n (21-127 kDa) investigated here has enabled observation of impact of molecular weight on the electronic structure of the acceptor polymer PNDIBS. It is to be noted that similar effects of M_n on electronic structure has been observed for the donor polymer poly(3-hexylthiophene) (P3HT);[61-63] however, previous studies of other NDI-based copolymers found the LUMO/HOMO energy levels to be virtually independent of the polymer molecular weight.[11, 14] Our observed shifts of the LUMO/HOMO energy levels with increasing M_n suggest that the higher molecular weight PNDIBS samples have either more intrachain disorder due to backbone twisting[62] or an increase in density of amorphous regions.[62-64]

Thin film absorption spectra of the series of DHAP-prepared PNDIBS of different number-average molecular weight (M_n) are presented in Figure 1c, and the numerical optical parameters are summarized in Table 1. As expected and in good agreement with previous reports,[18, 57] these absorption spectra have two characteristic peaks at ~400 nm and 710 – 718 nm, which represent the π-π* transition and the intramolecular charge transfer (ICT) bands, respectively. We note that the absorption

Table 1. Molecular Weight, Electronic Structure, and Optical Properties of Acceptor Polymer PNDIBS and Donor Polymer PBDB-T.

Polymer	M_n (kDa)	M_w (kDa)	PDI	λ_{max} (nm)	α_{max} (10^5 cm^{-1})	λ_{ICT} (nm)	λ_{onset} (nm)	$E_g^{opt.(a)}$ (eV)	E_{HOMO} (eV)	E_{LUMO} (eV)
PNDIBS 21 kDa	21	36	1.7	397	0.75	718	885	1.40	-5.70	-3.84
PNDIBS 52 kDa	52	172	3.3	398	1.01	715	873	1.42	-5.73	-3.83
PNDIBS 55 kDa	55	132	2.4	397	0.96	713	868	1.42	-5.72	-3.84
PNDIBS 66 kDa	66	172	2.6	397	0.97	711	859	1.44	-5.82	-3.80
PNDIBS 90 kDa	90	270	3.0	399	0.98	716	872	1.42	-5.80	-3.75
PNDIBS 127 kDa	127	292	2.3	397	1.17	711	870	1.42	-5.86	-3.80

(a)$E_g^{opt.} = 1240/\lambda_{onset}$

spectra of the DHAP-prepared PNDIBS have a slightly wider but molecular weight independent optical bandgap ($E_g^{opt.}$) of 1.42-1.44 eV (Table 1), which is very similar to that of the Stille-prepared PDNIBS with E_g^{opt} of 1.40 eV (Figure S9). Clearly, this suggests that the polymerization method has only marginal impact on the optical bandgap of this semiconducting polymer. However, subtle and gradual hypsochromic shift of the ICT band with increasing M_n from 21kDa to 66kDa is observed (Table 1), and this means that intramolecular charge transfer between the NDI electron-accepting moiety and the biselenophene electron-donating moiety is increasingly weakened by backbone distortion and conformational disorder with increasing polymer chain length.[65] The slight bathochromic shift in the ICT band observed in higher M_n samples (90kDa and 127kDa) signify significant chain aggregation at increasing M_n. Interestingly, we also observed that the absorption coefficient (α_{max}) increased monotonically with increasing M_n (Figure 1c) from 0.75 x 10^5 cm^{-1} at 21 kDa to 1.17 x 10^5 cm^{-1} at 127 kDa. The absorption coefficients of PNDIBS copolymers are much higher than other typical NDI-based copolymers due to increased backbone planarity, increased interchain overlap, and higher crystallinity.[5, 6, 57] The observed increase of the absorption coefficient α_{max} with increasing molecular weight can be explained by the increased solid-state packing density as a result of chain folding at the higher M_n. Although not previously explained, similar effects of molecular weight on absorption coefficient have been observed in other donor-acceptor conjugated copolymers.[10, 49, 66]

We characterized the electron transport properties of one of the present DHAP-prepared PNDIBS (21 kDa) by using organic field-effect transistors (OFETs) with bottom-gate top-contact architecture as detailed in the Experimental Method section. For comparison, we similarly characterized the field-effect electron mobility of the Stille-prepared PNDIBS. The transfer curves and output curves are shown in Figure S10 while the saturation region field-effect electron mobility (μ_e^{FET}) is presented in Table S2. The Stille-prepared PNDIBS films annealed at 170 ^{o}C showed an average μ_e^{FET} of 0.15 cm^2/Vs with an on/off current ratio (I_{on}/I_{off}) of 1 x 10^5 (Table S2). If the same

PNDIBS films annealed only at room temperature (25 ^{o}C) the field-effect electron mobility drops to 0.04 cm^2/Vs, which suggests that thermal annealing at high temperature enhances electron transport by the increased crystallinity and favorable intermolecular packing. The DHAP-prepared PNDIBS films annealed at 170 ^{o}C had an average μ_e^{FET} of 0.16 cm^2/Vs with an on/off current ratio (I_{on}/I_{off}) of 4 x 10^6 (Table S2), which is comparable to that of the Still-prepared PNDIBS. However, the over one order of magnitude enhancement in on/off current ratio is notable and an indication of some of the advantages of the DHAP method in synthesizing defect-free, high regioregularity, and high mobility semiconducting polymers.
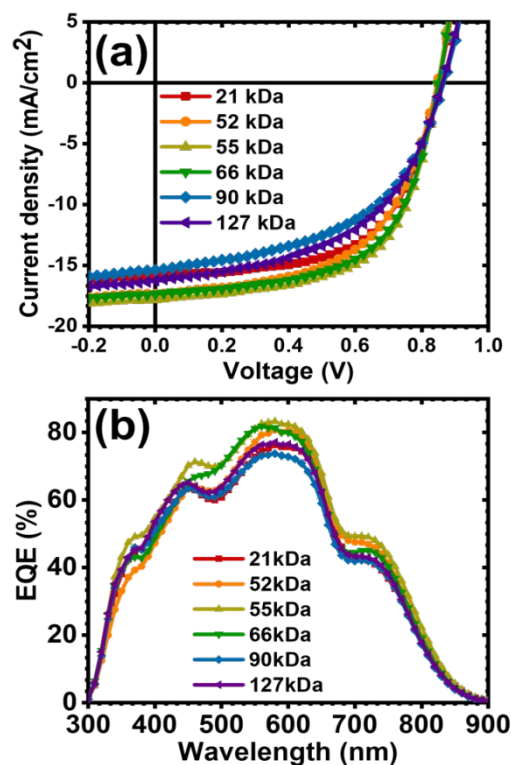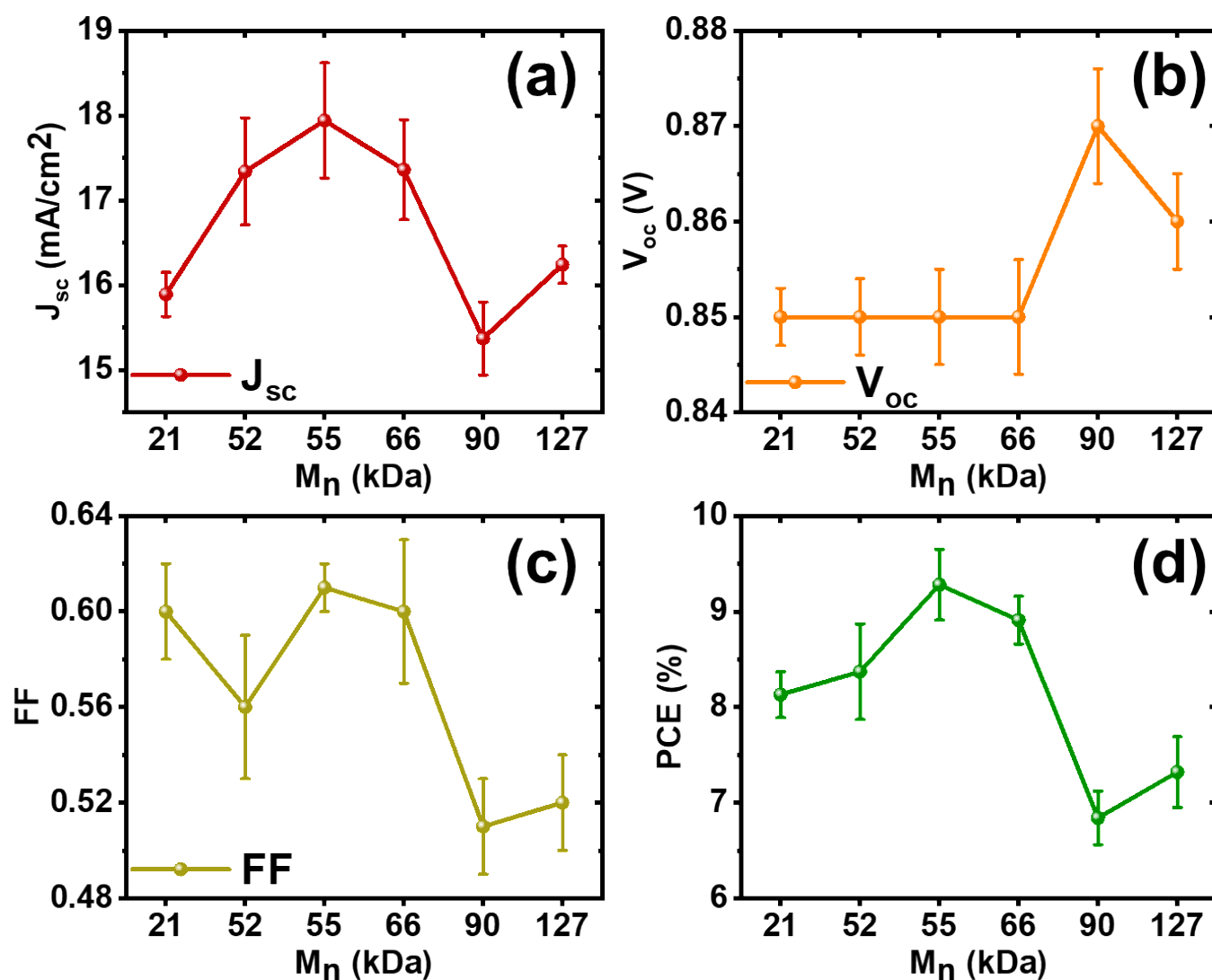

Figure 2. The acceptor polymer PNDIBS number-averaged molecular weight (M_n) dependence of photovoltaic properties of optimized PBDB-T:PNDIBS devices: (a) *J-V* curves; and (b) EQE spectra.

Table 2. Dependence of Photovoltaic Properties of Optimized PBDB-T:PNDIBS Blends on Acceptor Polymer PNDIBS Molecular Weight M_n.

Blend	J_{sc} (mA/cm^2)	V_{oc} (V)	FF	PCE$_{average}$[a] (%)	PCE$_{max}$ (%)	$J_{sc}$$^{calc.}$ (mA/cm^2)
PBDB-T:PNDIBS (21 kDa)	15.89 (± 0.26)	0.85 (± 0. 003)	0.60 (± 0. 02)	8.13 (± 0.24)	8.65	15.63
PBDB-T:PNDIBS (52 kDa)	17.34 (± 0.63)	0.85 (± 0. 004)	0.56 (± 0. 03)	8.37 (± 0.50)	9.12	16.35
PBDB-T:PNDIBS (55 kDa)	17.94 (± 0.68)	0.85 (± 0. 005)	0.61 (± 0. 01)	9.28 (± 0.37)	10.2	17.45
PBDB-T:PNDIBS (66 kDa)	17.36 (± 0.59)	0.85 (± 0. 006)	0.60 (± 0. 03)	8.91 (± 0.25)	9.35	16.50
PBDB-T:PNDIBS (90 kDa)	15.37 (± 0.43)	0.87 (± 0. 006)	0.51 (± 0. 02)	6.84 (± 0.28)	7.18	15.24
PBDB-T:PNDIBS (127 kDa)	16.24 (± 0.22)	0.86 (± 0. 005)	0.52 (± 0. 02)	7.32 (± 0.37)	8.12	15.84

[a]Average of over 10 devices

Figure 3. The relationships of photovoltaic parameters (J_{sc}, V_{oc}, FF, and PCE) with the number-averaged molecular weight M_n of acceptor polymer PNDIBS in PBDB-T:PNDIBS all-PSC devices: (a) J_{sc} vs. M$_n$, (b) V_{oc} vs. M_n, (c) FF vs. M_n, and (d) PCE vs. M_n. The error bars were generated from over 10 devices at each M_n.

Photovoltaic properties. We exploited the series of DHAP-prepared PNDIBS of different number-average molecular weight M_n to investigate the effects of the acceptor polymer M_n on the photovoltaic properties of all-PSCs. The photoactive layer of the devices thus comprised binary blend of the donor polymer PBDB-T and acceptor polymer PNDIBS. The all-PSCs were constructed with an inverted device architecture: ITO/ZnO/PEI/Blend/MoO$_3$/Ag, where polyethyleneimine (PEI) was used as a cathode interlayer.[67] The PBDB-T:PNDIBS blend devices were optimized by varying the donor polymer/acceptor polymer (D:A) ratio, annealing temperature, and use of solvent processing additives. The optimal processing conditions were found to be spin-coating of the blend solutions with D:A ratio of 1:0.8 wt/wt, thermal annealing at 110°C for 10 min, and *without* use of any solvent processing additive. The J-V responses and the EQE spectra of the optimized all-PSC devices for each PNDIBS molecular weight are presented in Figure 2 whereas the corresponding photovoltaic properties are summarized in Table 2. All the photovoltaic parameters, including J_{sc}, V_{oc}, FF, and PCE, are presented as a function of the PNDIBS molecular weight in Figure 3.

The dependence of J_{sc} on M_n, as shown in Figure 3a, exhibits a rise to a peak value at 55 kDa followed by a large decline. In particular, the photocurrent J_{sc} exhibits a peak of 17.94 mA/cm^2 at M_n of 55kDa, and subsequently decreases to a minimum value of 15.37 mA/cm^2 at 90 kDa before slightly rising again to 16.24 mA/cm^2 at 127 kDa (Table 2). As we will discuss later, further insights to this evolution of the photocurrent as a function of molecular weight can be gained by observed correlations with the blend charge transport properties, blend photophysics and blend film morphology. The V_{oc} as a function of M_n is relatively constant at $0.85 - 0.87$ V although a slight increase at the highest M_n values could be argued (Figure 3b); this observation is in agreement with the marginal changes in the LUMO energy level of PNDIBS as a function of molecular weight. The FF fluctuated around $0.60 - 0.64$ for M_n between 21 kDa to 66 kDa before decreasing to $0.51 - 0.53$ at higher M_n of 90-127 kDa (Figure 3c). These dependencies of the photovoltaic parameters J_{sc}, V_{oc}, and FF on M_n thus combined to produce the observed dependence of PCE on M_n shown in Figure 3d. The PCE rises with M_n to a maximum PCE of 10.2% at 55 kDa and significantly declines with further increases in M_n. Clearly, the M_n dependence of the PCE closely resembles the dependence of J_{sc} on molecular weight given the dominant role of the changes in photocurrent. Overall, we conclude from these observations that there exists an optimal or critical molecular weight of the acceptor polymer that optimizes the efficiency and photovoltaic properties of all-PSCs; the optimal value is in the range of 55-66 kDa in the case of the present PBDB-T:PNDIBS blend devices.

We note that the photovoltaic properties of a binary blend of donor polymer PBDB-T and a similarly DHAP-prepared PNDI2OD-T2 acceptor polymer of much higher M_n (M_n = 76kDa) (PCE = 7.3%)[53] are inferior to those of the PBDB-T:PNDIBS blends of lower PNDIBS M_n. This observation suggests the benefits of

moving from *bithiophene*-NDI copolymers to *biselenophene*-NDI copolymers.

The EQE spectra of the optimized devices for all M_n values investigated are shown in Figure 2b. The photocurrent response of all devices spanned the 885 nm to 300 nm range, which matched well with the complementary absorption spectra of the donor and the acceptor polymers in the PBDB-T:PNDIBS blends. Thus, it is clear that the photocurrent generated in the $460 - 670$ nm region comes from the photoinduced electron transfer from the donor polymer, whereas the photocurrent produced in the $350 - 460$ nm and $680 - 880$ nm regions originate from the photoinduced hole transfer from the acceptor polymer.[68] The maximum EQE value is found around $570 - 580$ nm for each M_n, varying from 73.7% for the 90kDa devices to 83.3% for the 55kDa, which mirrored the observed trend in J_{sc} (Figure 3a). Moreover, the optimized all-PSC devices fabricated from the optimal PNDIBS molecular weight of 52kDa $-$ 66kDa had superior quantum efficiency response throughout the whole spectral range, which is in good agreement with the observed enhanced J_{sc} at these M_n values. The photocurrent J_{sc} values obtained by integrating the EQE spectra were found to be within 2-6% mismatch with the values obtained directly from the J-V measurements (Table 2).

We found the photovoltaic properties of the all-PSCs at each molecular weight have different sensitivity towards the photoactive layer thickness. Thus, we chose all-PSC devices based on PNDIBS of 66 kDa and 90 kDa M_n values to probe the photoactive layer thickness dependence of the photovoltaic properties (Figure S11). The average PCE of the PNDIBS-66kDa devices is relatively constant at ~9.0% as the active layer thickness decreased from 100 nm to 80nm; the PCE decreased to ~8.0% as the thickness was further reduced to 70 nm. which was indicative of its weak dependence on the film thickness. In contrast, the efficiency of the PNDIBS-90kDa devices progressively increased from 5.4 to 7.3% as the active layer decreased from 110 nm to 70 nm. The much-improved photovoltaic properties of the 90 kDa devices at thinner active layers can be attributed to the strongly suppressed charge recombination and the reduced space-charge accumulation/formation. This observation suggests that blends of the higher molecular weight PNDIBS have potential applications in developing semi-transparent inverted all-polymer solar cells.

Charge Photogeneration and Charge Recombination. To investigate the effects of molecular weight of the acceptor polymer PNDIBS on the charge recombination kinetics, we characterized the J_{sc} and V_{oc} as a function of the incident light intensity (P_{light}). The dependency of V_{oc} on the light intensity can be generalized as $\frac{dV_{oc}}{dln(P_{light})} \propto s\frac{kT}{q}$, where k is the is the Boltzmann constant, T is temperature, and q is elementary charge. The value of the proportionality coefficient, s, is a measure of whether bimolecular recombination (s = 1) or trap-assisted recombination (s = 2) is dominant in the charge recombination dynamics.[69-71] The s value determined from the plot of V_{oc} versus ln (P_{light}) for all-PSC devices of different PNDIBS molecular weights (Figure 4a) varied from 1.02 in M_n of 21 kDa

to 1.15 in M_n of 127 kDa. Clearly, the near unity s coefficient measured at all the M_n values means that bimolecular recombination is the dominant charge recombination mechanism in these all-PSC blends.
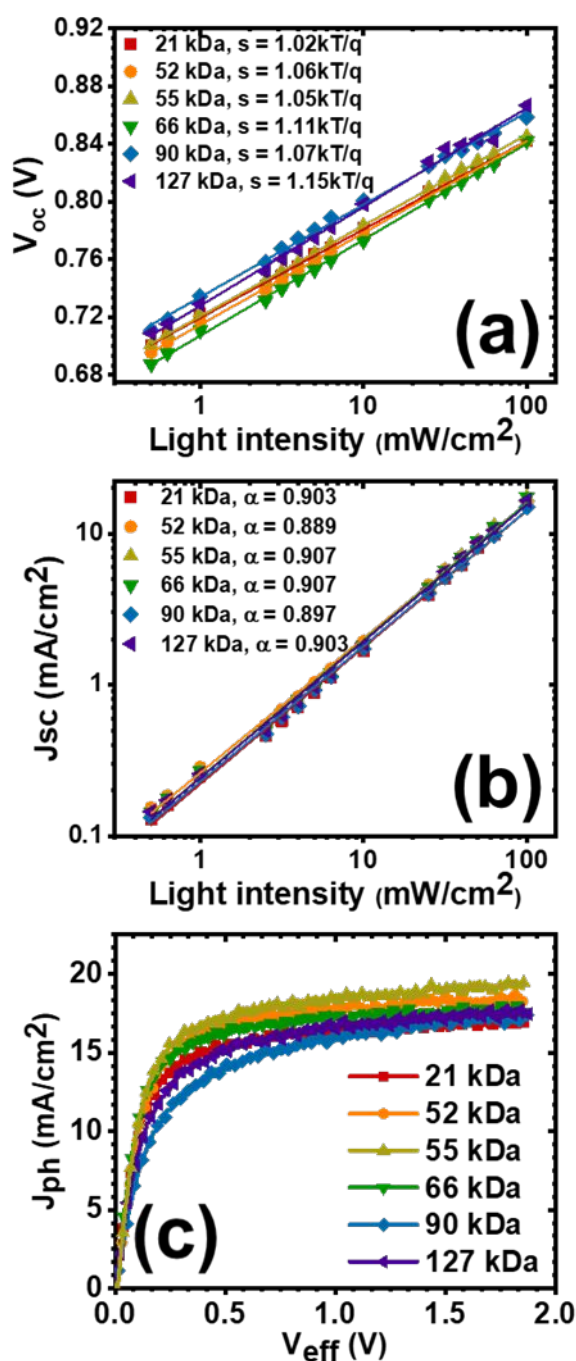

Figure 4. Dependence of photovoltaic parameters on incident light intensity for the optimized PBDB-T:PNDIBS devices of various acceptor polymer molecular weight M_n: (a) V_{oc} vs P_{light}; (b) J_{sc} vs P_{light}. (c) J_{ph} vs V_{eff} for optimized PBDB-T:PNDIBS devices of various acceptor polymer molecular weight M_n.

The relationship between J_{sc} and P_{light} can be modelled as $J_{sc} \propto P_{light}{}^{\alpha}$, where linearity ($\alpha = 1$) indicates that all charge carriers are collected at electrodes prior to recombination whereas significant deviation from linearity implies otherwise.[69, 71, 72] From the exponential coefficient α values

extracted from Figure 4b, we observed a significant deviation from unity for all devices at all of the M_n values ($\alpha = 0.897 - 0.907$). These results suggest the existence of severe bimolecular recombination in all-PSC devices from all PNDIBS molecular weights investigated. The slightly higher α value observed at 55kDa and 66kDa ($\alpha = 0.907$) might reflect weaker bimolecular recombination as suggested by the slight improvement in FF ($0.60 - 0.61$). Moreover, the much lower exponential coefficient especially in the 90kDa devices ($\alpha = 0.897$) coupled with the unbalanced charge transport to be discussed below suggest that the performance of these all-PSC devices is hindered not only by bimolecular recombination but also by space-charge effects;[72] we note that this observation is consistent with our observed enhanced efficiency in devices with thinner active layers discussed above. The high degree of bimolecular recombination in these blends is further confirmed by examining the trend of FF with respect to the incident light intensity. As shown in Figure S12a, the fill factor of the PBDB-T:PNDIBS devices at all M_n values increased with decreasing light intensity. This improvement in FF at low light intensity can be rationalized by the strongly suppressed bimolecular recombination due to decreased charge carrier density. Overall, these results demonstrate that the nature of charge recombination kinetics in these PBDB-T:PNDIBS devices is independent of the molecular weight of PNDIBS and that the all-PSCs are dominated by bimolecular recombination, which appears to lead to the relatively low FF values ($0.52 - 0.61$) when compared to other reported high-performing all-PSCs.

We investigated the molecular weight dependence of the charge generation kinetics of the present all-PSC devices by evaluating the maximum photoinduced charge photogeneration rate (G_{max}) and charge extraction rate ($P(E,T)$) via the relationship between the photocurrent ($J_{ph} = J_{light} - J_{dark}$, where J_{light} is the current density under illumination, and J_{dark} is the dark current density) and the effective voltage ($V_{eff} = V_o - V_a$, where V_o is the built-in voltage, and V_a is the applied voltage). The plot of J_{ph} versus V_{eff} is given in Figure 4c whereas the $P(E,T)$ and G_{max} values are summarized in Table S3. All the devices at all M_n values, with the exception of the 90kDa devices, showed saturated photocurrents at a relatively low effective voltage of 0.8V (Figure 4c). This observation suggest that apart from the 90kDa devices which exhibit a poor charge extraction probability of 89.3%, all photogenerated excitons in the all-PSCs at all other M_n values were essentially dissociated into free charge carriers that were effectively collected at the electrodes as evidenced by the high $P(E,T)$ under short-circuit condition ($93.7\% - 94.5\%$) (Table S3). The M_n dependence of the maximum charge photogeneration rate (G_{max}) was found to parallel the trend observed in the above photovoltaic properties and the blend charge transport properties discussed below. Specifically, the G_{max} rose from 1.06×10^{28} m^{-3}s^{-1} in the 21kDa devices, peaked at 1.21×10^{28} m^{-3}s^{-1} in the 55kDa devices, and then declined to 1.09×10^{28} m^{-3}s^{-1} in the 90-127kDa devices (Table S3). Since the thin film absorption coefficient was marginally affected by the polymer molecular weight, we conclude that the observed difference in the charge photogeneration rate as a function of M_n can be attributed

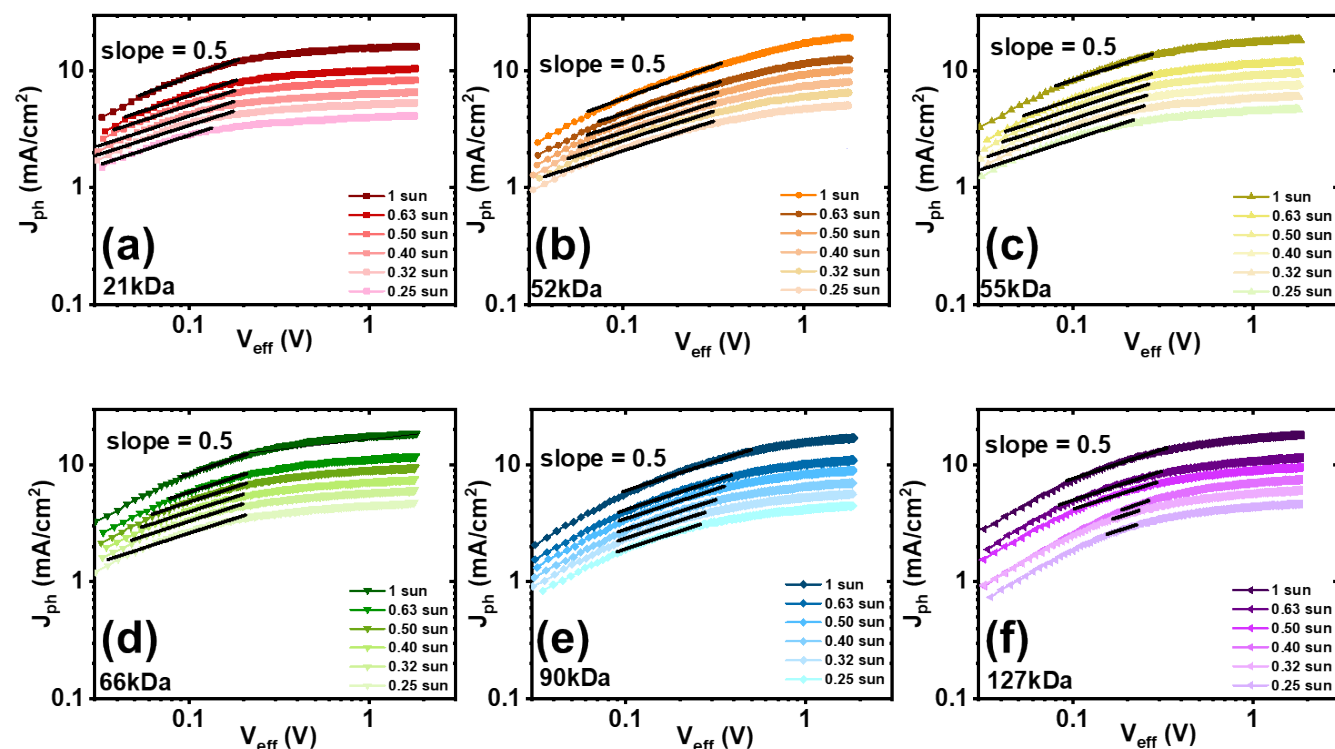primarily to the variation in morphology at the various molecular weights as will be discussed in detail below.

Figure 5. J_{ph} vs. V_{eff} for optimized PBDB-T:PNDIBS devices at various PNDIBS molecular weight and at different incident light intensity: (a) 21kDa, (b) 52kDa, (c) 55kDa, (d) 66kDa, (e) 90kDa, and (f) 127kDa.

To further confirm the formation of space-charge region (SCR) in the 90kDa and 127kDa blend devices, the relationship of J_{ph} and V_{eff} as a function of incident light intensity was characterized, and results for the optimized PBDB-T:PNDIBS devices of different M_n values are showed in Figure 5. The characteristic space-charge limited photocurrent is expected to have a square-root dependency on the effective voltage.[73] As shown in Figures 5a-5d, the SCR remained within V_{eff} of lower than 0.3V; thus, indicating that the formation of space-charge is relatively weak. On the other hand, the SCR in 90kDa and 127kDa devices extended to much higher V_{eff} of 0.4 − 0.5V (Figures 5e-5f). Moreover, the square-root region was found to persist and shift to lower V_{eff} at lower incident light intensity. These observations suggested that the space-charge formation in the 90kDa and 127kDa devices was more severe; thereby, explaining the poor photovoltaic properties and corroborating the increasing PCE at thinner films. The presence of space-charge effects can also be proved by investigating the dependency of saturation voltage (V_{sat}) extracted from Figures 5, which is the transition voltage from the saturation region to the square-root region, on the incident light intensity[73] as shown in Figure S12b. The V_{sat} of the optimized PBDB-T:PNDIBS devices fabricated from the lower molecular weight acceptor polymers (21kDa, 52kDa, 55kDa, and 66kDa) exhibited nearly independency on P_{light} where the slopes were found to be around 0.03 − 0.16; thus, suggesting weak space-charge

formation. The relationship of V_{sat} and P_{light} of the 90kDa and 127kDa devices showed a slope of 0.45 and 0.34, respectively, which is in good agreement with the theoretical prediction of space-charge region (slope = 0.5).[73] These analyses collectively confirm that there is significant space-charge formation in the 90kDa and 127kDa devices, which explain the decreased photovoltaic properties compared to the lower M_n based devices as observed earlier.

Table 3. Dependence of SCLC Charge Carrier Mobilities of Optimized PBDB-T:PNDIBS Blend Films on Acceptor Polymer PNDIBS Molecular Weight.

Blend	$\mu_{electron}$ (cm^2/Vs)	μ_{hole} (cm^2/Vs)	μ_{hole}/ $\mu_{electron}$
PBDB-T:PNDIBS (21kDa)	5.80×10^{-5}	1.91×10^{-4}	3.30
PBDB-T:PNDIBS (52kDa)	1.18×10^{-4}	3.06×10^{-4}	2.59
PBDB-T:PNDIBS (55kDa)	1.96×10^{-4}	3.21×10^{-4}	1.64
PBDB-T:PNDIBS (66kDa)	1.51×10^{-4}	1.81×10^{-4}	1.12
PBDB-T:PNDIBS (90kDa)	4.05×10^{-5}	1.25×10^{-4}	3.08
PBDB-T:PNDIBS (127kDa)	3.60×10^{-5}	1.14×10^{-4}	3.15

Charge Transport Properties of PBDB-T:PNDIBS Blend Films. We characterized the PNDIBS molecular weight (M_n)

dependence of bulk charge transport in the all-PSC devices by measuring the space-charge limited current (SCLC) charge carrier mobilities of PBDB-T:PNDIBS blend films processed at the same optimal conditions as used to fabricate the all-PSC devices. The J-V curves and SCLC fitting lines for hole-only devices and electron-only devices are shown in Figures S13 and S14, respectively. The M_n dependence of the electron mobility, the hole mobility (μ_h), and the ratio μ_h/μ_e for the PBDB-T:PNDIBS blend films are shown in Figure 6. Both μ_e and μ_h exhibit very similar trends, increasing to their peak values at 55 kDa and subsequently decreasing as the molecular weight increased to 127kDa (Figure 6). Specifically, the electron mobility of the blend films increased 3.4-fold from the 21 kDa value to a maximum of 1.96 x 10^{-4} cm²/Vs at 55kDa and then dropped to 3.60 x 10^{-5} cm²/Vs at 127 kDa (Table 3). On the other hand, the corresponding hole mobility of the blend films increased 1.7-fold from 1.91 x 10^{-4} cm²/Vs at 21 kDa to the peak value of 3.21 x 10^{-4} cm²/Vs at 55 kDa and then decreased to 1.14 x 10^{-4} cm²/Vs at 127 kDa (Table 3). These measured values of both hole and electron mobilities are comparable with previous reports for all-PSC devices containing the present donor and acceptor polymers.[18] Further analysis reveals that the blend charge transport becomes more symmetric with the μ_h/μ_e ratio approaching unity (μ_h/μ_e = 1.12 – 1.64) around the optimal molecular weight range of 55-66 kDa (Figure 6). The poor electron and hole mobilities accompanied by the highly asymmetric charge transport observed in the 90 kDa and127 kDa PBDB-T:PNDIBS blends is consistent with space-charge
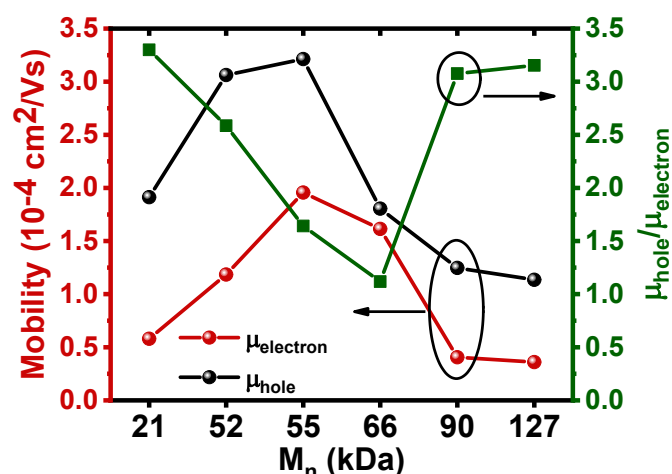

Figure 6. PNDIBS molecular weight (M_n) dependence of the space-charge limited current (SCLC) charge carrier mobilities of PBDB-T:PNDIBS blend films processed at the same optimal conditions used to fabricate the all-PSC devices.

effects and their observed inferior photovoltaic device performance. It is also clear that the higher carrier mobilities and more symmetric charge transport observed at the optimal molecular weight range (M_n = 55-66 kDa) are in good agreement with the higher J_{sc} and FF values observed in the photovoltaic properties discussed earlier.

Surface and Bulk Morphology. The PNDIBS molecular weight M_n dependence of the surface morphology of the PBDB-T:PNDIBS blend films was investigated by atomic force microscopy (AFM) imaging (Figure 7). The PBDB-T:PNDIBS blend

films of increasing PNDIBS molecular weight evolved from tightly spaced fibrils with small domain sizes of around 24 nm in the 21 kDa to a well-connected network of needle-like features having extended domains of about 30 – 40 nm (52, 55, and 66 kDa) to featureless structures with larger domains of approximately 50 nm (90 and 127 kDa) (Figure 7). Combining these observations with the earlier charge photogeneration analysis, it can be concluded that the PBDB-T:PNDIBS blends that exhibit intermediate domain sizes of around 30 – 40nm are more suitable for exciton dissociation and charge generation. Although the much finer phase separation seen in the 21kDa blends could facilitate efficient exciton diffusion and dissociation, the generated charges are more likely to encounter one another and recombine prior to being extracted and thereby limit the overall photogeneration rate. On the other hand, the larger-scale phase separation in the 90 kDa and 127 kDa blends could inhibit exciton diffusion to the donor/acceptor blend interface and thus hamper the charge photogeneration rate as well. These changes of the blend surface morphology suggest two transition points from the less aggregating (21 kDa) to crystalline and well-ordered domains (52 – 66 kDa) and subsequently to the more amorphous and highly disordered structures (90 – 127 kDa). The blend
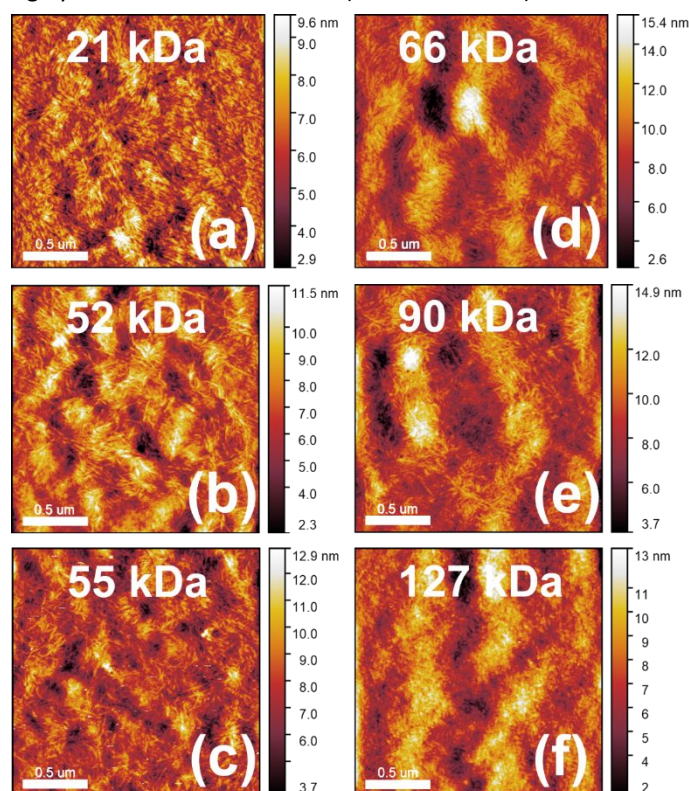

Figure 7. AFM height images (2μm x 2μm) of PBDB-T:PNDIBS blend films at various acceptor polymer PNDIBS molecular weight. All active layers were processed at the optimal conditions.

morphology evolution with molecular weight parallel observations in the M_n dependencies of photovoltaic and charge transport properties, where the highest efficiencies (PCEs) and largest charge carrier mobilities occurred only in

blends that exhibit intermediate domain sizes and well-ordered crystalline regions.

Two-dimensional (2D) grazing incident wide-angle X-ray scattering (2D-GIWAXS) measurements were carried out on the optimized PBDB-T:PNDIBS blend films of various PNDIBS molecular weights M_n. The 2D-GIWAXS images and the 1D line cuts for the PBDB-T:PNDIBS blend films are presented in Figure
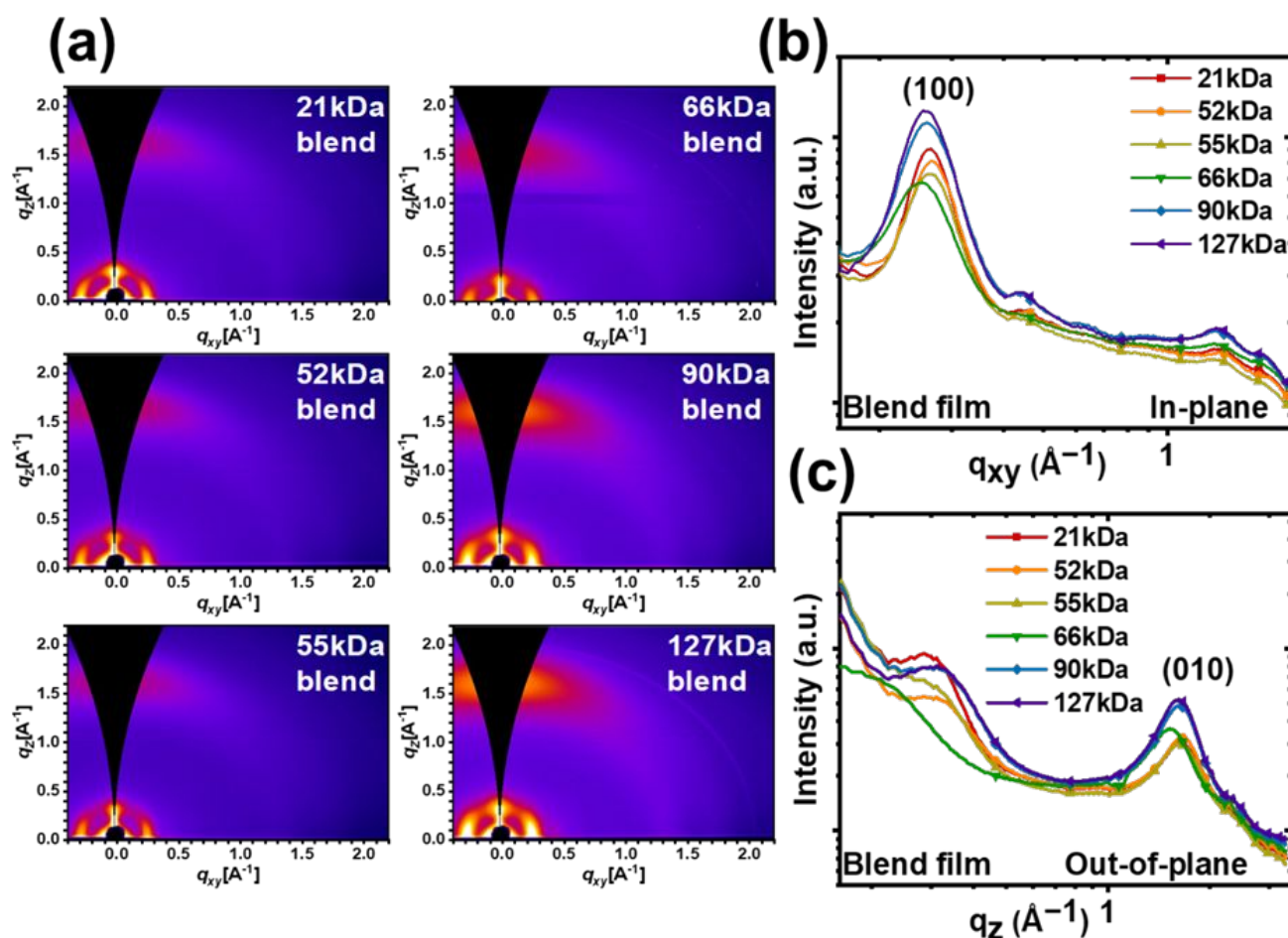

Figure 8. PNDIBS molecular weight dependence of 2D-GIWAXS data for PBDB-T:PNDIBS blend active layers processed at the optimal conditions: (a) 2D-GIWAXS patterns; (b, c) 1D line cuts of GIWAXS patterns in the in-plane (IP) (b) and the out-of-plane (OOP) direction (c).

8 and those for the neat PBDB-T films are given in Figure S15. All blend films exhibited pronounced (100) diffraction peaks in the in-plane (IP) direction at $q_{xy} = 0.25 - 0.27$ Å^{-1} (Table S4) which are similar to the values observed in the neat acceptor polymer thin films.[18] The higher order diffraction peaks (h00) which are characteristic of highly ordered PNDIBS had disappeared, which suggest that the polymer chain packing is less ordered upon blending with the donor polymer PBDB-T. In the out-of-plane (OOP) direction, a distinct (010) diffraction peak is observed at $q_z = 1.61 - 1.66$ Å^{-1} (Table S4) for all blend films except for the 66kDa blend film. Surprisingly, the (010) peak of the 66kDa blend film shifted to a much lower q_z of 1.52 Å^{-1}. The presence of the sharp and intense (100) peak and (010) peak in the IP and OOP directions (Figure 8), respectively, strongly indicate that the most crystallites in all of the PBDB-T:PNDIBS blends preferentially adopt the *face-on* orientation. Moreover, compared to the blend films of other molecular weights, the 55kDa and 66kDa blend films exhibited extremely broad and weak (100) diffraction peaks in the OOP direction.

These results suggest that among all of the blend films, the highest population of *face-on* oriented crystallites can be expected in the 55kDa and 66kDa blend films, which can explain their observed better charge transport (μ_e, μ_h, and μ_h/μ_e) and their improved photovoltaic parameters (J_{sc}, FF, and PCE).

The crystalline coherence length (L_c) estimated from the Scherrer's equation for all PBDB-T:PNDIBS blend films was found to decrease from 7.8 nm in the PNDIBS-21kDa blend (Table 4) to a minimum value of 5.5 nm in PNDIBS-66kDa blend (Table 4) and then rises to 6.5 nm in the PNDIBS-127kDa blend (Table 4 and Figure 9). Adding the M_n dependent photovoltaic

Table 4. Summary of d-spacing, π- π Distance, and Crystalline Coherence Length (L$_c$) Derived from In-Plane (IP) and Out-of-Plane (OOP) Line Cuts in 2-D GIWAXS of Blend Thin Films.

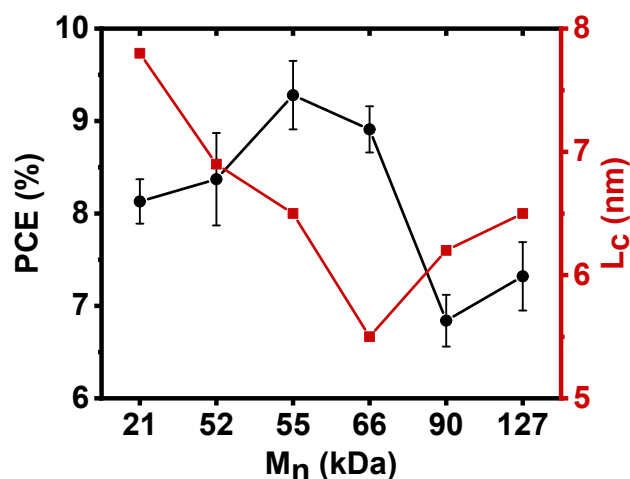| Polymer	d-spacing (Å)	π- π distance (Å)	L$_c$ (nm) (100) IP
PBDB-T	22.0	3.73	5.2
PBDB-T:PNDIBS (21kDa)	23.5	3.85	7.8
PBDB-T:PNDIBS (52kDa)	23.5	3.79	6.9
PBDB-T:PNDIBS (55kDa)	23.5	3.85	6.5
PBDB-T:PNDIBS (66kDa)	24.7	4.14	5.5
PBDB-T:PNDIBS (90kDa)	24.1	3.85	6.2
PBDB-T:PNDIBS (127kDa)	24.7	3.90	6.5

Figure 9. Dependencies of the power conversion efficiency (PCE) of PBDB-T:PNDIBS all-polymer solar cells and the blend crystal coherence length (L$_c$) on the acceptor polymer PNDIBS M_n.

efficiency to Figure 9 shows that the PCE and blend L$_c$ trends are related, suggesting that there are perhaps three distinct blend morphology regions that impact the performance of these all-PSCs devices. In the optimal M_n region of ~ 55-66kDa, the blend film exhibits a phase-separated bi-continuous morphology with intermediate nanocrystalline domains (L$_c$ ~ 5.5-6.5 nm) that enable good mixing of the donor and acceptor polymer counterparts, which in turn increases the donor/acceptor interfacial area and hence facilitates large exciton dissociation, charge photogeneration, and charge transport for overall enhanced PCE, J_{sc}, and FF. On the lower M_n side, the morphology is characterized by relatively large crystalline domains (L$_c$ ~ 7-8 nm), which while enabling good charge transport lacks sufficient donor/acceptor interfacial area and charge photogeneration essential to achieve optimal performance. At higher M_n (90-127kDa), although the crystalline coherence length remains moderate (L$_c$ ~ 6.2 − 6.5 nm), the morphology is dominated by large scale disordered microstructure evidenced by the featureless AFM images which lacked microfibrils (Figure 7). Consequently, blend devices at

these higher M_n values suffered from severe bimolecular recombination and space-charge effects mainly due to the poor charge transport properties and lower charge extraction rate, which explain the decrease in the photovoltaic properties (PCE, J_{sc}, and FF).

Conclusions

We have synthesized six well-defined number-average molecular weight (M_n) values (21-127 kDa) of the n-type semiconducting biselenophene-naphthalenediimide copolymer (PNDIBS) via direct heteroarylation polymerization (DHAP) and used them to investigated the influence of polymer molecular weight on the morphology, photophysics, charge transport, and photovoltaic properties of all-polymer solar cells (all-PSCs). Both short-circuit current (J_{sc}) and power conversion efficiency (PCE) of the PBDB-T:PNDIBS blend devices were found to increase with increasing M_n until they peaked at an optimal M_n of 55 kDa and thereafter decreased with further increases in M_n. The maximum and average PCE of 10.2% and 9.3%, respectively, observed at the optimal M_n value of 55 kDa coincided with optimal blend charge transport properties, blend photophysics, and blend morphology at this critical molecular weight. At the optimal M_n, the blend morphology was characterized by a bi-continuous network of 5.5-6.5 nm crystalline domains with predominantly *face-on* molecular orientations whereas on the higher M_n side a relatively disordered microstructure with larger scale phase separation was evident from 2D-GIWAXS and AFM imaging while a more finely packed crystalline microstructure was observed at 21 kDa. In particular, the observed decrease of photovoltaic parameters at higher M_n could be explained by the larger scale phase separation, decrease in electron mobility, severe bimolecular recombination, and formation of space-charge region. The sensitivity of the all-PSC device efficiency to the active layer thickness was found to depend on the acceptor polymer molecular weight. The PCE of devices at around the optimal M_n was relatively constant with active layer thickness whereas at the higher M_n the efficiency varied significantly with layer thickness, suggesting the potential of using the high molecular weight PNDIBS for semi-transparent all-PSC applications. Overall, the results of this study demonstrate the importance of tuning the molecular weight of the polymer components to optimize the morphology, charge transport, photophysics and efficiency of all-polymer solar cells. The results also provide new insights on structure-property relationships for the n-type semiconducting copolymer PNDIBS.

Conflicts of interest

There are no conflicts to declare.

Acknowledgements

References

1. C. Lee, S. Lee, G.-U. Kim, W. Lee and B. J. Kim, *Chem. Rev.*, 2019, **119**, 8028-8086.
2. G. Wang, F. S. Melkonyan, A. Facchetti and T. J. Marks, *Angew. Chem. Int. Ed.*, 2019, **58**, 4129-4142.
3. Z. Genene, W. Mammo, E. Wang and M. R. Andersson, *Adv. Mater.*, 2019, **31**, 1807275.
4. H. Benten, D. Mori, H. Ohkita and S. Ito, *J. Mater. Chem. A*, 2016, **4**, 5340-5365.
5. T. Earmme, Y.-J. Hwang, N. M. Murari, S. Subramaniyan and S. A. Jenekhe, *J. Am. Chem. Soc.*, 2013, **135**, 14960-14963.
6. T. Earmme, Y.-J. Hwang, S. Subramaniyan and S. A. Jenekhe, *Adv. Mater.*, 2014, **26**, 6080-6085.
7. Y.-J. Hwang, T. Earmme, S. Subramaniyan and S. A. Jenekhe, *Chem. Commun.*, 2014, **50**, 10801-10804.
8. Y.-J. Hwang, B. A. E. Courtright, A. S. Ferreira, S. H. Tolbert and S. A. Jenekhe, *Adv. Mater.*, 2015, **27**, 4578-4584.
9. Y.-J. Hwang, T. Earmme, B. A. E. Courtright, F. N. Eberle and S. A. Jenekhe, *J. Am. Chem. Soc.*, 2015, **137**, 4424-4434.
10. H. Kang, M. A. Uddin, C. Lee, K.-H. Kim, T. L. Nguyen, W. Lee, Y. Li, C. Wang, H. Y. Woo and B. J. Kim, *J. Am. Chem. Soc.*, 2015, **137**, 2359-2365.
11. J. Jung, W. Lee, C. Lee, H. Ahn and B. J. Kim, *Adv. Energy Mater.*, 2016, **6**, 1600504.
12. L. Gao, Z.-G. Zhang, L. Xue, J. Min, J. Zhang, Z. Wei and Y. Li, *Adv. Mater.*, 2016, **28**, 1884-1890.
13. Z. Li, X. Xu, W. Zhang, X. Meng, W. Ma, A. Yartsev, O. Inganäs, M. R. Andersson, R. A. J. Janssen and E. Wang, *J. Am. Chem. Soc.*, 2016, **138**, 10935-10944.
14. N. Zhou, A. S. Dudnik, T. I. N. G. Li, E. F. Manley, T. J. Aldrich, P. Guo, H.-C. Liao, Z. Chen, L. X. Chen, R. P. H. Chang, A. Facchetti, M. Olvera de la Cruz and T. J. Marks, *J. Am. Chem. Soc.*, 2016, **138**, 1240-1251.
15. Z.-G. Zhang, Y. Yang, J. Yao, L. Xue, S. Chen, X. Li, W. Morrison, C. Yang and Y. Li, *Angew. Chem. Int. Ed.*, 2017, **56**, 13503-13507.
16. Z. Li, X. Xu, W. Zhang, X. Meng, Z. Genene, W. Ma, W. Mammo, A. Yartsev, M. R. Andersson, R. A. J. Janssen and E. Wang, *Energy & Environ Sci.*, 2017, **10**, 2212-2221.
17. B. Fan, L. Ying, P. Zhu, F. Pan, F. Liu, J. Chen, F. Huang and Y. Cao, *Adv. Mater.*, 2017, **29**, 1703906.
18. N. B. Kolhe, H. Lee, D. Kuzuhara, N. Yoshimoto, T. Koganezawa and S. A. Jenekhe, *Chem. Mater.*, 2018, **30**, 6540-6548.
19. X. Liu, C. Zhang, C. Duan, M. Li, Z. Hu, J. Wang, F. Liu, N. Li, C. J. Brabec, R. A. J. Janssen, G. C. Bazan, F. Huang and Y. Cao, *J. Am. Chem. Soc.*, 2018, **140**, 8934-8943.
20. X. Xu, Z. Li, J. Wang, B. Lin, W. Ma, Y. Xia, M. R. Andersson, R. A. J. Janssen and E. Wang, *Nano Energy*, 2018, **45**, 368-379.
21. X. Xu, Z. Li, W. Zhang, X. Meng, X. Zou, D. Di Carlo Rasi, W. Ma, A. Yartsev, M. R. Andersson, R. A. J. Janssen and E. Wang, *Adv. Energy Mater.*, 2018, **8**, 1700908.
22. K. D. Deshmukh, R. Matsidik, S. K. K. Prasad, L. A. Connal, A. C. Y. Liu, E. Gann, L. Thomsen, J. M. Hodgkiss, M. Sommer and C. R. McNeill, *Adv. Funct. Mater.*, 2018, **28**, 1707185.
23. J. Yuan, M. J. Ford, Y. Xu, Y. Zhang, G. C. Bazan and W. Ma, *Adv. Energy Mater.*, 2018, **8**, 1703291.
24. K. Zhang, R. Xia, B. Fan, X. Liu, Z. Wang, S. Dong, H.-L. Yip, L. Ying, F. Huang and Y. Cao, *Adv. Mater.*, 2018, **30**, 1803166.
25. H. Yao, F. Bai, H. Hu, L. Arunagiri, J. Zhang, Y. Chen, H. Yu, S. Chen, T. Liu, J. Y. L. Lai, Y. Zou, H. Ade and H. Yan, *ACS Energy Lett.*, 2019, **4**, 417-422.
26. N. B. Kolhe, D. K. Tran, H. Lee, D. Kuzuhara, N. Yoshimoto, T. Koganezawa and S. A. Jenekhe, *ACS Energy Lett.*, 2019, **4**, 1162-1170.
27. H. Sun, Y. Tang, C. W. Koh, S. Ling, R. Wang, K. Yang, J. Yu, Y. Shi, Y. Wang, H. Y. Woo and X. Guo, *Adv. Mater.*, 2019, **31**, 1807220.
28. J. Wu, Y. Meng, X. Guo, L. Zhu, F. Liu and M. Zhang, *J. Mater. Chem. A*, 2019, **7**, 16190-16196.
29. T. Jia, J. Zhang, W. Zhong, Y. Liang, K. Zhang, S. Dong, L. Ying, F. Liu, X. Wang, F. Huang and Y. Cao, *Nano Energy*, 2020, **72**, 104718.
30. Y. Wu, S. Schneider, C. Walter, A. H. Chowdhury, B. Bahrami, H.-C. Wu, Q. Qiao, M. F. Toney and Z. Bao, *J. Am. Chem. Soc.*, 2020, **142**, 392-406.
31. K. Feng, J. Huang, X. Zhang, Z. Wu, S. Shi, L. Thomsen, Y. Tian, H. Y. Woo, C. R. McNeill and X. Guo, *Adv. Mater.*, 2020, **32**, 2001476.
32. Q. Fan, R. Ma, T. Liu, W. Su, W. Peng, M. Zhang, Z. Wang, X. Wen, Z. Cong, Z. Luo, L. Hou, F. Liu, W. Zhu, D. Yu, H. Yan and E. Wang, *Sol. RRL*, 2020, **4**, 2000142.
33. J. Du, K. Hu, L. Meng, I. Angunawela, J. Zhang, S. Qin, A. Liebman-Pelaez, C. Zhu, Z. Zhang, H. Ade and Y. Li, *Angew. Chem. Int. Ed.*, 2020, **n/a**.
34. D. K. Tran, N. B. Kolhe, Y.-j. Hwang, D. Kuzuhara, T. Koganezawa and S. A. Jenekhe, *ACS Appl. Mater. Interfaces*, 2020, **12**, 16490-16502.
35. Q. Fan, W. Su, S. Chen, W. Kim, X. Chen, B. Lee, T. Liu, U. A. Mendez-Romero, R. Ma, T. Yang, W. Zhuang, Y. Li, Y. Li, T.-S. Kim, L. Hou, C. Yang, H. Yan, D. Yu and E. Wang, *Joule*, 2020, **4**, 658-672.
36. Y. Meng, J. Wu, X. Guo, W. Su, L. Zhu, J. Fang, Z.-G. Zhang, F. Liu, M. Zhang, T. P. Russell and Y. Li, *Sci. China Chem.*, 2019, **62**, 845-850.
37. Y. Xu, J. Yuan, S. Zhou, M. Seifrid, L. Ying, B. Li, F. Huang, G. C. Bazan and W. Ma, *Adv. Funct. Mater.*, 2019, **29**, 1806747.
38. S. Lee, Y. Kim, Z. Wu, C. Lee, S. J. Oh, N. T. Luan, J. Lee, D. Jeong, K. Zhang, F. Huang, T.-S. Kim, H. Y. Woo and B. J. Kim, *ACS Appl. Mater. Interfaces*, 2019, **11**, 45038-45047.
39. Y. Zhang, Y. Xu, M. J. Ford, F. Li, J. Sun, X. Ling, Y. Wang, J. Gu, J. Yuan and W. Ma, *Adv. Energy Mater.*, 2018, **8**, 1800029.
40. T. Kim, J.-H. Kim, T. E. Kang, C. Lee, H. Kang, M. Shin, C. Wang, B. Ma, U. Jeong, T.-S. Kim and B. J. Kim, *Nat. Commun.*, 2015, **6**, 8547.
41. J.-W. Lee, B. S. Ma, J. Choi, J. Lee, S. Lee, K. Liao, W. Lee, T.-S. Kim and B. J. Kim, *Chem. Mater.*, 2020, **32**, 582-594.
42. J. Choi, W. Kim, S. Kim, T.-S. Kim and B. J. Kim, *Chem. Mater.*, 2019, **31**, 9057-9069.
43. Q. Zhang, X. Yuan, Y. Feng, B. W. Larson, G. M. Su, Y. Maung Maung, N. Rujisamphan, Y. Li, J. Yuan and W. Ma, *Sol. RRL*, 2020, **4**, 1900524.
44. Y. Xu, J. Yuan, S. Liang, J.-D. Chen, Y. Xia, B. W. Larson, Y. Wang, G. M. Su, Y. Zhang, C. Cui, M. Wang, H. Zhao and W. Ma, *ACS Energy Lett.*, 2019, **4**, 2277-2286.
45. J. Yuan, Y. Zhang, L. Zhou, G. Zhang, H.-L. Yip, T.-K. Lau, X. Lu, C. Zhu, H. Peng, P. A. Johnson, M. Leclerc, Y. Cao, J. Ulanski, Y. Li and Y. Zou, *Joule*, 2019, **3**, 1140-1151.
46. Y. Cui, H. Yao, J. Zhang, T. Zhang, Y. Wang, L. Hong, K. Xian, B. Xu, S. Zhang, J. Peng, Z. Wei, F. Gao and J. Hou, *Nat. Commun.*, 2019, **10**, 2515.
47. S. Liu, J. Yuan, W. Deng, M. Luo, Y. Xie, Q. Liang, Y. Zou, Z. He, H. Wu and Y. Cao, *Nat. Photonics*, 2020, **14**, 300-305.
48. J. Yuan, Y. Xu, G. Shi, X. Ling, L. Ying, F. Huang, T. H. Lee, H. Y. Woo, J. Y. Kim, Y. Cao and W. Ma, *J. Mater. Chem. A*, 2018, **6**, 10421-10432.

49. S. Chen, Y. An, G. K. Dutta, Y. Kim, Z.-G. Zhang, Y. Li and C. Yang, *Adv. Funct. Mater.*, 2017, **27**, 1603564.

50. B. Fan, L. Ying, Z. Wang, B. He, X.-F. Jiang, F. Huang and Y. Cao, *Energy & Environ Sci.*, 2017, **10**, 1243-1251.

51. D. Qian, L. Ye, M. Zhang, Y. Liang, L. Li, Y. Huang, X. Guo, S. Zhang, Z. a. Tan and J. Hou, *Macromolecules*, 2012, **45**, 9611-9617.

52. T. Bura, J. T. Blaskovits and M. Leclerc, *J. Am. Chem. Soc.*, 2016, **138**, 10056-10071.

53. A. Robitaille, S. A. Jenekhe and M. Leclerc, *Chem. Mater.*, 2018, **30**, 5353-5361.

54. T. Bura, S. Beaupre, M.-A. Legare, J. Quinn, E. Rochette, J. T. Blaskovits, F.-G. Fontaine, A. Pron, Y. Li and M. Leclerc, *Chem. Sci.*, 2017, **8**, 3913-3925.

55. P.-O. Morin, T. Bura, B. Sun, S. I. Gorelsky, Y. Li and M. Leclerc, *ACS Macro Lett.*, 2015, **4**, 21-24.

56. M. Wakioka, N. Ichihara, Y. Kitano and F. Ozawa, *Macromolecules*, 2014, **47**, 626-631.

57. Y.-J. Hwang, G. Ren, N. M. Murari and S. A. Jenekhe, *Macromolecules*, 2012, **45**, 9056-9062.

58. S. Shi, J. Yuan, G. Ding, M. Ford, K. Lu, G. Shi, J. Sun, X. Ling, Y. Li and W. Ma, *Adv. Funct. Mater.*, 2016, **26**, 5669-5678.

59. Y. Ito, A. A. Virkar, S. Mannsfeld, J. H. Oh, M. Toney, J. Locklin and Z. Bao, *J. Am. Chem. Soc.*, 2009, **131**, 9396-9404.

60. P. Espinet and A. M. Echavarren, *Angew. Chemie. Int. Ed.* , 2004, **43**, 4704-4734.

61. W. C. Tsoi, S. J. Spencer, L. Yang, A. M. Ballantyne, P. G. Nicholson, A. Turnbull, A. G. Shard, C. E. Murphy, D. D. C. Bradley, J. Nelson and J.-S. Kim, *Macromolecules*, 2011, **44**, 2944-2952.

62. S. Ko, E. T. Hoke, L. Pandey, S. Hong, R. Mondal, C. Risko, Y. Yi, R. Noriega, M. D. McGehee, J.-L. Bredas, A. Salleo and Z. Bao, *J. Am. Chem. Soc.*, 2012, **134**, 5222-5232.

63. S. Sweetnam, K. R. Graham, G. O. Ngongang Ndjawa, T. Heumuller, J. A. Bartelt, T. M. Burke, W. Li, W. You, A. Amassian and M. D. McGehee, *J. Am. Chem. Soc.*, 2014, **136**, 14078-14088.

64. R. Noriega, J. Rivnay, K. Vandewal, F. P. V. Koch, N. Stingelin, P. Smith, M. F. Toney and A. Salleo, *Nat. Mater.*, 2013, **12**, 1038-1044.

65. H. Li, Y.-J. Hwang, B. A. E. Courtright, F. N. Eberle, S. Subramaniyan and S. A. Jenekhe, *Adv. Mater.*, 2015, **27**, 3266-3272.

66. J. J. Intemann, K. Yao, H.-L. Yip, Y.-X. Xu, Y.-X. Li, P.-W. Liang, F.-Z. Ding, X. Li and A. K. Y. Jen, *Chem. Mater.*, 2013, **25**, 3188-3195.

67. B. A. E. Courtright and S. A. Jenekhe, *ACS Appl. Mater. Interfaces*, 2015, **7**, 26167-26175.

68. G. Ren, C. W. Schlenker, E. Ahmed, S. Subramaniyan, S. Olthof, A. Kahn, D. S. Ginger and S. A. Jenekhe, *Adv. Funct. Mater.*, 2013, **23**, 1238-1249.

69. C. M. Proctor, M. Kuik and T.-Q. Nguyen, *Prog. Polym. Sci.*, 2013, **38**, 1941-1960.

70. L. J. A. Koster, V. D. Mihailetchi, R. Ramaker and P. W. M. Blom, *Appl. Phys. Lett.*, 2005, **86**, 123509.

71. S. R. Cowan, N. Banerji, W. L. Leong and A. J. Heeger, *Adv. Funct. Mater.*, 2012, **22**, 1116-1128.

72. L. J. A. Koster, V. D. Mihailetchi, H. Xie and P. W. M. Blom, *Appl. Phys. Lett.*, 2005, **87**, 203502.

73. V. D. Mihailetchi, J. Wildeman and P. W. M. Blom, *Phys. Rev. Lett.*, 2005, **94**, 126602.

Table of Contents Entry

This work provides a unified understanding on how polymer molecular weight influences the blend photophysics, blend morphology, charge transport, and photovoltaic properties of all-polymer solar cells.